

Learning and predicting respiratory motion from 4D CT lung images

11

T. He, Z. Xue

Houston Methodist Research Institute, Houston, TX, United States

CHAPTER OUTLINE

11.1 Introduction	335
11.2 3D/4D CT Lung Image Processing	339
11.2.1 Lung Field and Vessel Segmentation	339
11.2.2 Serial Image Segmentation and Registration	342
11.3 Extracting and Estimating Motion Patterns From 4D CT	346
11.3.1 A Lung Motion Estimation Framework	346
11.3.2 Motion Estimation Models	348
11.3.3 Experiments	350
11.4 An Example for Image-Guided Intervention	352
11.4.1 CTF Guidance With Motion Compensation	352
11.4.2 The CT-CTF Registration Algorithm	353
11.4.3 Experiments	356
11.5 Concluding Remarks	358
Acknowledgment	359
References	359

11.1 INTRODUCTION

In radiology, interventional radiology, radiation therapy and surgery, medical imaging techniques have been widely used for capturing structural and functional images of human body/organs for diagnosis, treatment planning, and guidance of treatments. Medical imaging provides images of internal organs that are not directly accessible (Smith and Kim, 2011; Jacob et al., 2000; Klein et al., 1995) and, from these

images, physicians can gather anatomical and functional information and interpret the pathological conditions of patients. Using computer-assisted diagnosis (CAD) tools, quantitative measures of pathological conditions such as lesion, tumor, blood flow, calcification, organ/tissue size and thickness, cardiac structural and functional dysfunctions, as well as brain connectivity can be collected to help perform diagnosis. Meanwhile, images of these conditions can help plan procedures such as intervention, radiotherapy, and surgery. Follow-up studies can also be performed to assess the treatment response, for example, radiotherapy and chemotherapy outcomes, recurrence of cancer, neuroradiological assessment of developmental and degenerative diseases.

Advances in imaging equipment have facilitated the development of new effective and efficient treatment options, converting complex open surgeries to possible minimally invasive procedures, shortening patients' recovery time, improving patient comfort, and eliminating the risk of complications. Minimally invasive intervention is now replacing more costly open surgery in oncology, neurology, pulmonology, and cardiology (Sadeghi Naini et al., 2010; Seinstra et al., 2010; Ukimura, 2010; de Gregorio et al., 2008; Yeung et al., 2006; DeLucia et al., 2006; Shamir et al., 2005; Westendorff et al., 2004; Cleary et al., 2002; Broaddus et al., 2001; Hall et al., 2001; Seibel, 1997; Yaniv et al., 2010; Cleary and Peters, 2010; Enquobahrie et al., 2008, 2007; Sun et al., 2006). During minimally invasive procedures clinicians rely on imaging patients and tracking of interventional devices and combining the device location with their knowledge of patients' anatomy and pathological conditions to build up a mental picture to direct their actions. Software fusion and visualization of images and devices together provide an effective tool to help physicians perform the procedure. In a typical interventional procedure, first a diagnostic or preprocedural image, such as computed tomography (CT) or magnetic resonance imaging (MRI), is captured for planning. Image segmentation and visualization tools can be used at this stage to highlight the details of pathological conditions and to plan the procedure (such as defining the entrance point and trajectory path for biopsy). In radiotherapy planning, tumor(s) are segmented precisely to define the gross tumor volume (GTV), the clinical target volume (CTV) and the planning target volume (PTV), and radiation beams are optimized to maximizing desired radiation doses to the tumor, while minimizing the damage to surrounding normal tissues. Then during radiotherapy, the planning data are automatically registered onto the intraprocedural images to guide the delivery of radiation beams. Typically, in image-guided procedures it is desirable that a real-time imaging technique can provide patients' anatomy information and track device location on-site. Ultrasound is preferred because it is real-time and without radiation exposure. However, ultrasound may have some limitations such as limited tissue contrast. Intraprocedural CT or CT fluoroscopy (CTF) are also often used but they may not be sufficient for dynamic organs, such as lung and cardiac imaging. Similar problems are also encountered in radiation therapy, and we are lacking real-time or radiation-free imaging devices to track the patients' motion.

To date, ultrasound is the most widely used real-time imaging modality for visualizing patients' anatomy in soft-tissue organs such as the breasts, liver, kidney, and prostate (Sadeghi Naini et al., 2010; Bouchet et al., 2001; Karnik et al., 2010;

Park et al., 2010). What is more, during intervention the device (needle) is also visible by ultrasound imaging. This makes it convenient for use by interventional radiologists, and in fact ultrasound is one of the most popular imaging techniques for guidance. But the disadvantage of ultrasound is that the echo signals are not as clear as CT and MRI for tissue structures. Many real-time image fusion methods can be used to register a preprocedure CT or MRI onto the ultrasound image, so that by superimposing the registered image onto the ultrasound images, the structures can be clearly visualized. Additionally, ultrasound also has limitations in assessing the lungs and deep organs because of the reflection on the tissue-air interface, the effect of rib bones, and lack of image contrast inside the lungs (Park et al., 2010).

Other real-time imaging modalities such as endoscopy, X-rays (Lin et al., 2009), and real-time MR (Cervino et al., 2011) can also be used for guidance. For example, in bronchoscopy or colonoscopy endoscope cameras are used for real-time visualization; in vascular intervention real-time X-ray or fluoroscopy coupled with contrast agents are used to highlight the vessels; in operation open MR is used to get real-time anatomy images (of the brain). While endoscopy gives real-time videos and fluoroscopy obtains real-time 2D projection images, they largely rely on clinicians' skills for navigating the device to the target. Concerns for fluoroscopy are that they provide only local 2D projection images and expose both clinicians and patients to radiation. To incorporate more global information, preprocedural 3D CT can be registered with 2D fluoroscopy images so not only local or 2D real-time feedback but also global 3D visualization about where the devices are located can be provided. On the other hand, although it is possible to perform image-guided intervention within open MR scanners, it is not commonly used in clinics due to the cost of the machine time and the complicated clinical setup that requires all devices to be MRI compatible (Seimenis et al., 2012; Yakar et al., 2011; Lang et al., 2011; Tokuda et al., Jan 2010; Pandya et al., 2009; Patriciu et al., 2007; DiMaio et al., 2007).

Besides the above-mentioned real-time imaging techniques, tracking of interventional devices is another task in order to visualize them in the context of anatomy. The most commonly used tracking techniques of interventional devices include electromagnetic (EM) tracking and optical tracking (Shah et al., 2011; Cala et al., 1996; Li et al., 2011). For EM tracking coil sensors are installed within the interventional devices so that their positions can be tracked in real-time within the human body covered by a magnetic field. For optical tracking, markers can be attached to the device allowing its position to be tracked with a stereo vision system by assuming the device is rigid. Other tracking techniques are being developed so that the interventional devices can be tracked within the imaging equipment. For example, coil-based sensors can be installed on the needle tip and radio-frequency signals can be detected using an MR machine while the intervention procedure is performed.

The key for image-guided procedures is to visualize the patient's anatomy and operative devices simultaneously in real-time. However, as mentioned above, real-time imaging may not be available together with device tracking in clinics. For example, in percutaneous lung intervention electromagnetic or optical tracking can be used for detecting the interventional probes, but there is a lack of real-time imaging

technique for navigation. A similar situation also exists in lung cancer radiotherapy. The major problem herein is that using static preprocedural CT is not able to solve the discrepancies between the CT and the patient's respiratory stage. Thus for lung cancer treatment, monitoring respiratory phases has been the major focus in dealing with breathing or poor reproducibility of breath-holding.

It is in this context that motion compensation becomes a major task for accurate guidance: it is highly desirable that a precise lung motion model can be used as the roadmap for guiding the intervention during each breath-holding cycle. Recent advances in motion estimation show that by using regression models or machine learning methods it is possible to estimate the lung motion from partially measurable signals such as chest motion signals. In the literature, there are many works dealing with lung motion, and they can be classified into three categories. The first is lung motion deformation modeling with registration ([Sundaram et al., 2004](#); [Vandemeulebroucke et al., 2011](#); [Handels et al., 2007](#)), but they only construct the respiratory patterns and do not achieve motion modeling/estimation. The second uses an individual patient's dataset ([Wu et al., 2011](#)), for example, first extracting lung motion in preprocedural 4D scans and then applying this model during treatment (radiotherapy or intervention), where 4D scanning is required. Finally, a statistical model can be applied to incorporate both group and individual information for motion modeling. Respiratory patterns trained from a large number of subjects can be used to guide the estimation of dynamic images of individuals, even when the 4D CT images are not available for them ([Klinder et al., 2010](#); [Ehrhardt et al., 2011](#)). For example, one can use the motion of a patient's external features in combination with a motion model to compensate for internal respiratory motion ([Lu et al., 2006](#); [Santelli et al., 2011](#); [He et al., 2010](#)). The challenge is that the limited dimension of respiratory sensor signals may not reflect the high-dimensional lung motion accurately, and although they monitor respiratory phases well, they may not estimate accurate lung tumor location and shape dynamics. With new machine learning and estimation technologies, the noncontact vision-based motion monitoring devices can be used for detecting the high-dimensional chest surface motion ([Tan et al., 2010](#)), and it would be promising to estimate dynamic lung motion by statistical model-based prediction between high-dimensional chest surface and lung motion vectors.

In this chapter, we introduce a method to estimate dynamic lung images from the 3D CT and high-dimensional chest surface signals. This estimation framework consists of two stages: the training and the estimating stages. In the training stage, after performing longitudinal registration of the 4D CT data of each training subject, the respiratory motion fields are calculated. Then all the images, motion fields, and chest surface motions of each subject are aligned onto a template space for training a statistical model. The relationship between the chest surface motion and lung respiratory motion is then established in the template space by using prediction or regression algorithms. During the motion estimation stage, the chest surface motion signals and the 3D CT of a patient will be captured and transformed to the template space through image registration, and we can apply the motion prediction model trained above to estimate patient-specific lung field motion from the chest surface

signals. Finally, the estimated dynamic lung images are transformed back to the patient image space.

The chapter is organized according to the key steps of this motion estimation framework. First, we will discuss 3D and 4D CT lung image processing including segmentation and registration, which act as the key steps used to extract lung motion, in [Section 11.2](#). Then we introduce the motion estimation method, which aims to model the relationship between the lung motion fields with the chest surface motion signals, in [Section 11.3](#). Finally, in [Section 11.4](#) we give an example of how the motion estimation can be used in a CTF-guided lung intervention system to register the patient's diagnostic CT image onto the real-time captured CTFs during an interventional procedure. [Section 11.5](#) is the conclusion of this chapter.

11.2 3D/4D CT LUNG IMAGE PROCESSING

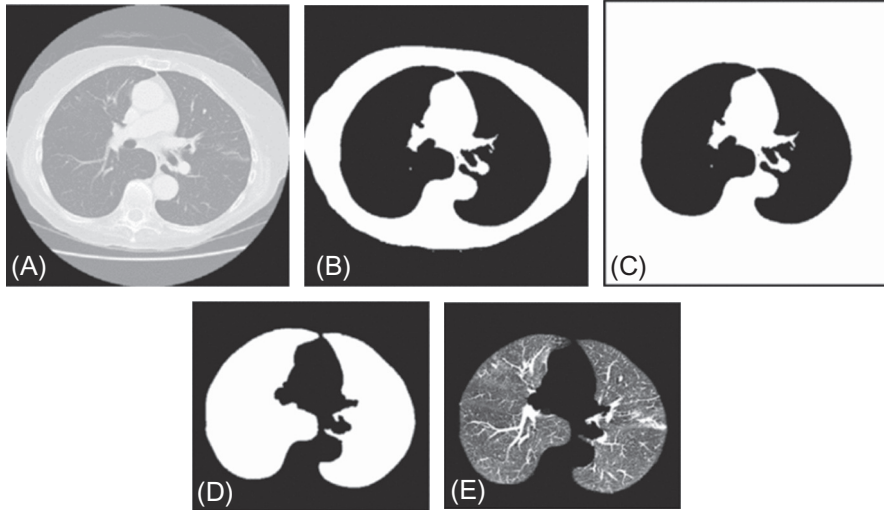
In this section two important steps for CT lung image processing, segmentation and registration, are introduced. After presenting lung field and vessel segmentation, we describe a joint image segmentation and registration algorithm for 4D images. This processing is essential for extracting longitudinal respiratory motion vectors and shape information for motion estimation.

11.2.1 LUNG FIELD AND VESSEL SEGMENTATION

11.2.1.1 Lung field extraction

Lung field extraction is a critical preprocessing stage in lung segmentation to separate the cavity, lung field, and free space from the input CT images. Many subsequent processes such as vessel segmentation and tumor segmentation utilize this step as initial preprocessing. For example, the segmented lung field provides a bounding area for vessel segmentation, and subsequently lung field surface motion can be used to characterize respiratory motion of the lung.

The lung field extraction method consists of the following two steps. First, the rough lung area is extracted using 3D region growing. In CT, since the inner lung field and airways have much lower density than pulmonary vessels and surrounding thoracic cavity, density-based segmentation methods like gray-level thresholding and region growing are generally used ([Sluimer et al., 2006](#)). The inverse operation of 3D region growing is an effective method of CT lung image segmentation ([Yim and Hong, 2008](#)). Therefore we start segmenting the thoracic cavity using region growing as follows: getting several seeds and extracting the chest wall by region growing; separating the air background using a similar region growing method. The seeds are selected automatically from the image boundary with intensities close to zero (points in the air). Then binary morphology and connected components analysis ([Hu et al., Jun 2001](#)) are applied to address the boundary indentations and bulges and to fill the cavities inside the lung area. Finally, the original CT image is masked by the binary lung field.

**FIG. 11.1**

Segmentation of lung field. (A) Input CT image. (B) 3D region growing on chest wall. (C) 3D region growing on air background. (D) Inverting region growing result and performing morphology and connected components analysis. (E) Masking the lung image to extract the lung field.

Fig. 11.1 shows an example of lung field segmentation. We can see that by first segmenting the chest wall and the empty space surrounding the patient, the lung field area can be filtered. Further morphological operations can help clean up and fine-tune the binary mask of the lung field.

11.2.1.2 Vessel segmentation using geometric active contour models

Precise segmentation of pulmonary vessels from CT lung images provides vital visualization for interventional guidance to avoid major vessel damage. It is also important to align the vessel structures when performing intra- and intersubject image registration, particularly in motion estimation of the lung. While simple thresholding and window/level setting can briefly segment different tissues, their results are not accurate because of the intensity variation. Recent studies showed that level-set methods have been successfully used in image segmentation. Let us look at the traditional level-set method (Osher and Sethian, 1988). Briefly, the evolving surface $c(t)$ that separates the object and background is represented by a propagating front embedded as the zero level-set of function $\psi(\mathbf{x}, t)$, such that $c(t) = \{\mathbf{x} | \psi(\mathbf{x}, t) = 0\}$. \mathbf{x} represents an image voxel. The evolution rule for $\psi(\mathbf{x}, t)$ is

$$\frac{\partial \psi}{\partial t} + F |\nabla \psi| = 0. \quad (11.1)$$

The velocity function F is dependent on the image data and the current level-set function ψ . ψ is usually defined as the signed distance function (SDF), and it deforms iteratively according to F . Malladi et al. (1995) proposed a simple formulation for F :

$$F = g \cdot (v - \theta k), \quad (11.2)$$

where θ indicates an external propagation force leading to the surface contraction or expansion uniformly based on its sign. k is the local curvature of the evolving front. θ controls the influence of the curvature and acts as a regularization term to smooth out the high curvature part of the surface. g is the data consistency term. In image segmentation, if one needs to halt the evolution of the surface at object boundaries, g can be created as an edge stopping function as

$$g = \frac{1}{1 + |\nabla G_\sigma * I_{\mathbf{x}}|}. \quad (11.3)$$

In implementation, the front can propagate by updating the level-set function in its neighborhood, so we can only update ψ in a narrow band around the front surface.

11.2.1.3 Vascularity-oriented level-set (VOLES)

When applying the geometric active contour method in vessel segmentation, we encountered a major obstacle in propagating the zero level-set along the vessel direction. This is because the high curvature will receive a high penalty on the evolving front in order to yield a smooth surface of the objects, which makes the propagation slower along tubular structures than in blob structures. To solve this problem, Lorigo et al. (2001) extended level-set segmentation to higher codimension: an underlying vector field is developed for driving the curve evolution in 3D. On the other hand, vessel enhancement filters also attracted more attention. The vesselness measure based on the eigensystem of the Hessian matrix of image intensity has been one of the most popular methods, and it can be combined with various image matching approaches to detect and identify vascular structures (Masutani et al., 2001; Descoteaux et al., 2008). Combining the ideas of using different curvature penalty and the vesselness enhancement, we proposed a new strategy called VOLES that applies vesselness-based compensation on the curvature penalty of the traditional level-set. The advantage is that the evolving front can move faster along the vessel directions, while still maintaining smoothness on the vessel walls.

Notice that θ in Eq. (11.2) controls the influence of the curvature, but when using it to propagate the front inside vascular structures, the front grows much more slowly along the vessels due to the larger curvature along the vessel directions. Fig. 11.2 shows such cases. In VOLES, we adopt the vesselness measure (Frangi et al., 1998), which is small along the vessel boundary and becomes larger near the centerline. Hence θ is now weighted according to this vascularity-oriented information:

$$\frac{\partial \psi}{\partial t} + g \cdot (v - \theta \cdot k) |\nabla \psi| = 0. \quad (11.4)$$

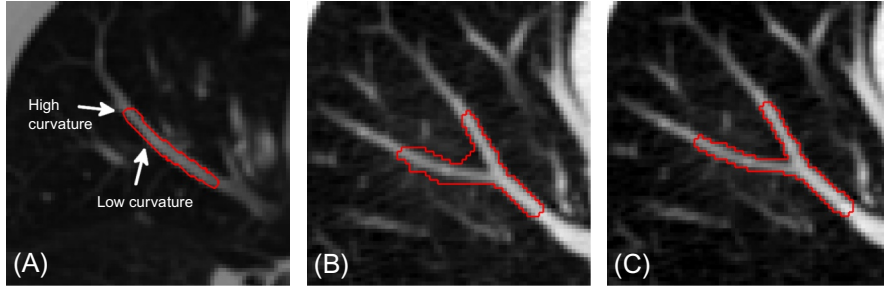
**FIG. 11.2**

Illustration of vessel propagation. (A) Different curvatures at different locations. (B) The same criterion results in slow grow along vessels and overflow in other regions. (C) Application of different constraints adaptively.

The curvature influence parameter θ is designed to be weighted by the vesselness measure V as

$$\theta = \alpha \cdot e^{(-\beta V)^3}. \quad (11.5)$$

Vesselness V is large along the vessel direction where local curvature k is large, and in this case θ will be smaller to compensate the penalty of the large curvature. As shown in Fig. 11.2C, the propagation of the level-set will be faster along the vessel direction. Similarly, the vesselness measure can also be applied to the edge stopping function g ,

$$g = \frac{1}{1 + |\nabla G_\sigma * V_{\mathbf{x}}|}. \quad (11.6)$$

This allows more curvature penalty when the front is near the boundary. Finally, the external propagation force that determines the local propagation direction at each point of the front is defined as

$$v = \text{sign} \{ \Lambda_o p_o(I, V) - \Lambda_i p_i(I, V) \}. \quad (11.7)$$

Instead of using a single method, either expanding or contracting the surface, we classify each point of the current surface $c(t)$ and let it expand if it locally belongs to (inside) the vessel or contract if it does not (Hall et al., 2001). $p(I, V)$ stands for a 2D distribution of image intensity and vesselness for the local regions either inside or outside $c(t)$.

11.2.2 SERIAL IMAGE SEGMENTATION AND REGISTRATION

Simultaneous serial image segmentation and registration methods have been studied for several image modalities (Wang et al., 2006; Xiaohua et al., 2005; Xue

et al., 2006). The advantage is that segmentation can improve longitudinal image registration and longitudinal deformation fields can improve segment consistency of the serial images. This section introduces joint serial image registration and segmentation, wherein serial images are segmented based on the current temporal deformations so that the temporally corresponding tissues tend to be segmented into the same tissue type, and at the same time temporal deformations among the serial images are iteratively refined based on the updated segmentation results.

11.2.2.1 4D registration

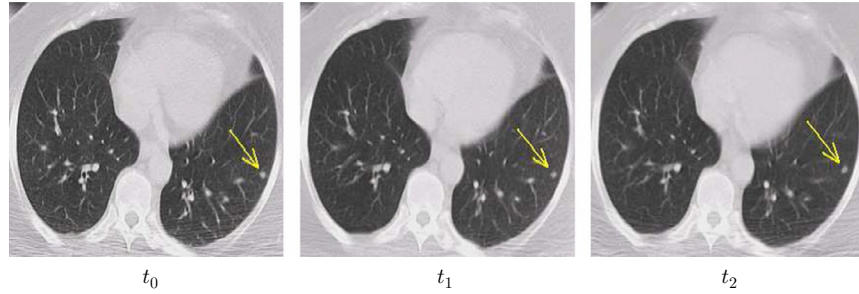
Given a series of images $I_{t=1,\dots,T}$, where I_1 is the baseline, the goal for serial image registration is to obtain the longitudinal deformation. We assume that the serial images have been globally aligned onto the baseline by applying rigid registration. To estimate the deformations from the baseline onto each image, that is, $\mathbf{f}_{1 \rightarrow t}$ or simplified as \mathbf{f}_t , registration needs to be performed. Since no longitudinal information is used in traditional pairwise registration or group-wise registration, temporal stability of the resultant serial deformations cannot be preserved. For example, in group-wise registration if one registers all the subsequent images onto the first image, no temporal information such as motion has been used and there are no temporal constraints between \mathbf{f}_t and \mathbf{f}_{t+1} , for example. Therefore to better use the temporal motion information we formulate the serial image registration in such a way that the registration of the current time-point image is related not only to the previous but also the following images (if available). No longitudinal smoothness constraints are applied to the serial deformations so that our algorithm can tolerate temporal anatomical and tissue property changes.

For the current image at time-point t , I_t , if the deformation of its previous image I_{t-1} , \mathbf{f}_{t-1} , and that of the next image I_{t+1} , \mathbf{f}_{t+1} , are known, the serial registration can be achieved by minimizing the following energy function:

$$E_{s,t}() = \sum_{\mathbf{x} \in \Omega} \left\{ |e(I_t(\mathbf{x} + \mathbf{f}_t(\mathbf{x}))) - e(I_1(\mathbf{x}))|^2 + \sum_{i=-1,1} |e(I_{t+i}(\mathbf{x} + \mathbf{f}_{t+i}(\mathbf{x}))) - e(I_t(\mathbf{x} + \mathbf{f}_t(\mathbf{x})))|^2 \right\} + E_r(\mathbf{f}_t(\mathbf{x})), \quad (11.8)$$

where $\mathbf{e}()$ is the operator for calculating image feature vectors and Ω is the image domain. The feature vector for each voxel consists of the intensity, gradient magnitude, and segmented tissue types, that is, $\mathbf{e}(\mathbf{x}) = [I(\mathbf{x}), \nabla I(\mathbf{x}), \mu_1(\mathbf{x}), \dots, \mu_C(\mathbf{x})]$. E_r is the regularization energy of the deformation field, and it can be derived from the prior distribution of the deformation. If no prior distribution is available, the regularization term can be some continuity and smoothness constraints. When cubic B-spline is used to model the deformation field, the continuity and smoothness are guaranteed, thus the regularization term E_r is omitted.

The serial image registration algorithm then iteratively calculates the deformation field \mathbf{f}_t at each time-point by minimizing the energy function in Eq. (11.8) until convergence. Notice that in the first iteration, since the registration results for neighboring images are not available, a pairwise registration can be used for

**FIG. 11.3**

Registered images of an image series.

initialization. Fig. 11.3 shows three consequent images after registration. It can be seen that the nodule has been aligned at the same position.

11.2.2.2 4D segmentation

Notice that in Eq. (11.8) $\mathbf{e}()$ stands for the image features extracting operator. It has been shown that by incorporating segmentation results such as tissue type, registration can be made more robust. With the estimated longitudinal deformation, 4D segmentation can be more accurate by applying the constraints that longitudinally corresponding voxels are likely to be segmented into the same tissue type; on the other hand, the same tissue types are likely to correspond longitudinally in order to refine the longitudinal deformation fields. Thus the purpose of the 4D segmentation is to calculate the segmented images by considering not only the spatial but also the temporal neighborhoods. A 4D clustering algorithm is used to classify each voxel of the serial image into C different tissue types by minimizing the objective function,

$$E(\mu, c) = \sum_{t=1}^T \sum_{\mathbf{x} \in \Omega} \left\{ \sum_{k=1}^C \left[\mu_{(t,\mathbf{x}),k}^q (I_{t,\mathbf{x}} - c_{t,k})^2 \right] + \frac{\alpha}{2} \rho_{(t,\mathbf{x})}^{(s)} \sum_{k=1}^C \left[\mu_{(t,\mathbf{x}),k}^q \bar{\mu}_{(t,\mathbf{x}),k}^{(s)} \right] + \frac{\beta}{2} \rho_{(t,\mathbf{x})}^{(t)} \sum_{k=1}^C \left[\mu_{(t,\mathbf{x}),k}^q \bar{\mu}_{(t,\mathbf{x}),k}^{(t)} \right] \right\}, \quad (11.9)$$

where voxel \mathbf{x} in image I_1 corresponds to voxel $\mathbf{x} + \mathbf{f}_t(\mathbf{x})$ in image I_t , referred to as voxel $(t, \mathbf{x}) = \mathbf{x} + \mathbf{f}_t(\mathbf{x})$, and μ, c, q, C follow the fuzzy c-mean (FCM) clustering formulation. We choose $C = 4$ so the tissue types include bone, background, and low/high-intensity soft tissue. $\bar{\mu}_{(t,\mathbf{x}),k}^{(s)}$ and $\bar{\mu}_{(t,\mathbf{x}),k}^{(t)}$ are the spatial and temporal neighborhood average membership functions and are defined as

$$\begin{aligned}
\bar{\mu}_{(t,\mathbf{x}),k}^{(s)} &= \frac{1}{N_1} \sum_{(t,\mathbf{u}) \in N_{(t,\mathbf{x})}^{(s)}} \sum_{m \in M_k} \mu_{(t,\mathbf{u}),m}^q \text{ and } \bar{\mu}_{(t,\mathbf{x}),k}^{(t)} \\
&= \frac{1}{N_2} \sum_{(\tau,\mathbf{w}) \in N_{(t,\mathbf{x})}^{(t)}} \sum_{m \in M_k} \mu_{(\tau,\mathbf{w}),m}^q, m,
\end{aligned} \tag{11.10}$$

where $N_{(t,\mathbf{x})}^{(s)}$ and $N_{(t,\mathbf{x})}^{(t)}$ are the spatial and temporal neighborhoods of voxel (t, \mathbf{x}) and $M_k = \{m = 1, \dots, C; m \neq k\}$. The fuzzy membership functions $\mu_{(t,\mathbf{x}),k}$ are subject to $\sum_{k=1}^C \mu_{(t,\mathbf{x}),k} = 1$, for all t and \mathbf{x} . The second term of Eq. (11.9) reflects the spatial constraints of the fuzzy membership functions. The difference is that an additional weight $\rho_{(t,\mathbf{x})}^{(s)}$ is used as an image-adaptive weighting coefficient, thus stronger smoothness constraints are applied in the image regions that have more uniform intensities, and vice versa. $\rho_{(t,\mathbf{x})}^{(s)}$ is defined as $\rho_{(t,\mathbf{x})}^{(s)} = \exp \left\{ -\sum_r \left[(D_r * I_t)_{(t,\mathbf{x})}^2 / 2\sigma_s^2 \right] \right\}$, where $(D_r * I_t)_{(t,\mathbf{x})}$ refers to first calculating the spatial convolution and then taking its value at location (t, \mathbf{x}) , and D_r is a spatial differential operator along axis r . Similarly, the third term of Eq. (11.9) reflects the temporal consistency constraints, and $\rho_{(t,\mathbf{x})}^{(t)}$ is calculated as $\rho_{(t,\mathbf{x})}^{(t)} = \exp \left\{ -(D_t * I_{(t,\mathbf{x})})_{(t)}^2 / 2\sigma_t^2 \right\}$. It is worth noting that the temporal smoothness constraint herein does not mean that the serial deformations have to be smooth across different time-points.

Using Lagrange multipliers to enforce the constraint of fuzzy membership function in the objective function, we get the following two equations to iteratively update the fuzzy membership functions and calculate the clustering centroids:

$$\mu_{(t,\mathbf{x}),k} = \frac{\left[(I_{(t,\mathbf{x})} - c_{t,k})^2 + \alpha \rho_{(t,\mathbf{x})}^{(s)} \bar{\mu}_{(t,\mathbf{x}),k}^{(s)} + \beta \rho_{(t,\mathbf{x})}^{(t)} \bar{\mu}_{(t,\mathbf{x}),k}^{(t)} \right]^{\frac{-1}{q-1}}}{\sum_{m=1}^C \left[(I_{(t,\mathbf{x})} - c_{t,m})^2 + \alpha \rho_{(t,\mathbf{x})}^{(s)} \bar{\mu}_{(t,\mathbf{x}),m}^{(s)} + \beta \rho_{(t,\mathbf{x})}^{(t)} \bar{\mu}_{(t,\mathbf{x}),m}^{(t)} \right]^{\frac{-1}{q-1}}} \tag{11.11}$$

and

$$c_{t,k} = \frac{\sum_{\mathbf{x} \in \Omega} \mu_{(t,\mathbf{x}),k}^q I_{(t,\mathbf{x})}}{\sum_{\mathbf{x} \in \Omega} \mu_{(t,\mathbf{x}),k}^q}. \tag{11.12}$$

Fig. 11.4 shows an example of the 4D segmentation results for serial CT lung images. To iteratively perform the joint registration and segmentation algorithm, the segmented images are used together with image intensities and image intensity gradients as the feature vector $\mathbf{e}()$ to refine the longitudinal deformations. The advantage of the joint algorithm is that the temporal consistency can be improved to recover the longitudinal deformations. Moreover, no temporal smoothness about the deformation fields is enforced in order to tolerate larger or discontinuous temporal changes that often appear during image-guided diagnosis and treatment. In the experiments no anatomical information such as blood vessels are used for the 4D registration. Future works include combining sophisticated segmentation to better represent the lung information for more robust registration.

**FIG. 11.4**

Sample 4D segmentation results.

11.3 EXTRACTING AND ESTIMATING MOTION PATTERNS FROM 4D CT

11.3.1 A LUNG MOTION ESTIMATION FRAMEWORK

In this section, we introduce the framework of dynamic lung image estimation. The algorithm is based on the idea that the relationship between lung motion and chest signals can be learned from a number of 4D CT samples of different subjects. Once the prediction model is established, for a new patient whose 3D CT and chest signals are available, we can use this respiratory motion prediction model to estimate the patient-specific respiratory motion.

Fig. 11.5 shows the framework for lung motion estimation. The algorithm consists of training and prediction stages. In the training stage, 4D CT images from a number of subjects are segmented, and their 4D motion fields are extracted by performing intrasubject registration. Then these images are registered onto a template subject. After registration, the relationship between the chest motion signals extracted and the entire lung motion fields is trained using a machine learning algorithm. For example, we can train a joint distribution between the 4D deformation fields and the chest motion signals, and their relationship can be estimated by either using a regression model or the Bayesian estimation algorithm. In the motion prediction stage, the 3D CT and chest motion vectors of a new subject are obtained and registered onto the same template space. Then the trained motion estimation model is applied to generate a series of lung deformations based on the chest surface motion vectors. These estimated lung deformations are transferred onto the patient space to generate a series of 3D images from the patient's 3D CT.

For intrasubject registration, the joint 4D segmentation and registration algorithm described in Section 11.2 is used to improve temporal consistency of motion vectors. Lung fields and vessels are also segmented as additional anatomical information to be used for the registration. For subject s , after registration, the longitudinal deformations $\mathbf{f}_{1 \rightarrow 2}^s, \mathbf{f}_{1 \rightarrow 3}^s, \dots, \mathbf{f}_{1 \rightarrow T}^s$ for serial images $I_1^s, I_2^s, \dots, I_T^s$ with T respiratory phases are obtained. To register the 4D respiratory motion fields of each subject onto the template, the baseline (first) image of the subject s and that of the template M , I_1^s and

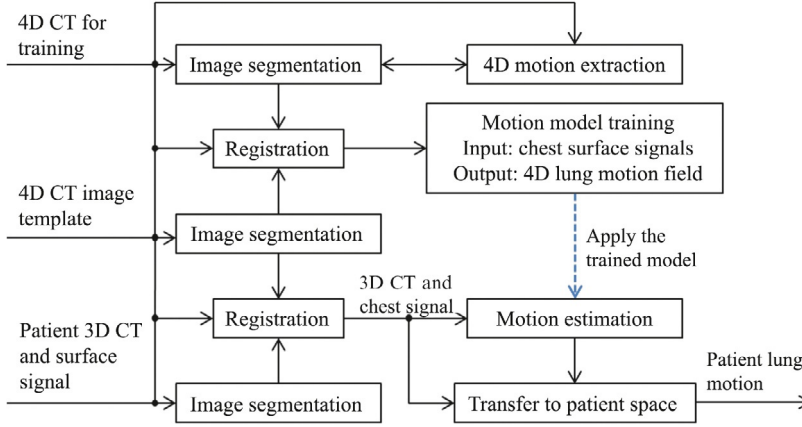


FIG. 11.5

The framework of the proposed 4D CT estimation algorithm.

I_1^M , are registered (Alexander et al., 2001), resulting in a global affine transformation $G_{M \rightarrow s}$ and a deformation field $\mathbf{f}_{M \rightarrow s}$. Therefore the baseline of the subject can be first transformed using $G_{M \rightarrow s}^{-1}$ (inverse of $G_{M \rightarrow s}$) and then deformed onto the template space based on the field $\mathbf{f}_{M \rightarrow s}$. To transform the respiratory motion fields of subject s onto the template space, we need to maintain the original motion patterns. Thus the global and local reorientation transformations between the subject and the template are applied to $\mathbf{f}_{1 \rightarrow 2}^s, \mathbf{f}_{1 \rightarrow 3}^s, \dots, \mathbf{f}_{1 \rightarrow T}^s$ to reflect the respiratory motion of the same subject on the template space. Denoting $g_{M \rightarrow s}$ as the global reorientation matrix of $G_{M \rightarrow s}$ without translation, whose inverse is $g_{M \rightarrow s}^{-1}$, the respiratory motion of subject s can be calculated first by $\mathbf{f}_{1 \rightarrow t}^{s'} = g_{M \rightarrow s}^{-1} \mathbf{f}_{1 \rightarrow t}^s, t = 2, \dots, T$, and then by performing a local reorientation:

$$\mathbf{u}_{1 \rightarrow t}^s(\mathbf{x}) = R_{M \rightarrow s}^{-1}(\mathbf{x}) \mathbf{f}_{1 \rightarrow t}^{s'}(\mathbf{x} + \mathbf{f}_{M \rightarrow s}(\mathbf{x})), \quad (11.13)$$

where $R_{M \rightarrow s}(\mathbf{x})$ is the local rotation matrix at a template voxel \mathbf{x} , calculated from the Jacobian matrix $J_{M \rightarrow s}(\mathbf{x})$ of $\mathbf{f}_{M \rightarrow s}(\mathbf{x})$ as $D_{M \rightarrow s}(\mathbf{x}) = ID + J_{M \rightarrow s}(\mathbf{x})$ (ID refers to the identity matrix), ie

$$R_{M \rightarrow s}(\mathbf{x}) = (D_{M \rightarrow s}(\mathbf{x}) D_{M \rightarrow s}^T(\mathbf{x}))^{-1/2} D_{M \rightarrow s}(\mathbf{x}). \quad (11.14)$$

In this way, all the longitudinal deformation fields calculated from the 4D CT training samples are transformed onto the template space. Similar operations are applied to the chest surface motion vectors, denoted as $\mathbf{v}_{1 \rightarrow t}^s, t = 2, \dots, T$. The goal of the motion estimation is therefore to estimate the relationship between $\mathbf{v}_{1 \rightarrow t}^s$ and $\mathbf{u}_{1 \rightarrow t}^s$ for all the respiratory phases $t = 1, \dots, T$.

For a new subject/patient P , we need to first determine which respiratory phase the input 3D CT belongs to. This can be determined by using its associated chest motion

signals. By performing smoothness filtering and detecting the exhale and inhale phases from the chest motion signals and dividing such signals into M phases, the phase of the synchronized 3D CT is determined. Without loss of generalization, let us assume the 3D CT corresponds to the first phase of the template image. Registering the patient data with the template image results in the global affine transformation $G_{M \rightarrow P}$ (reverse is $G_{P \rightarrow M}$) and deformation field $\mathbf{f}_{M \rightarrow P}$ (reverse is $\mathbf{f}_{P \rightarrow M}(\mathbf{x})$). In a similar way, the chest motion vectors of the patient can be transferred onto the template space, which can be denoted as $\mathbf{v}_{1 \rightarrow t}^P, t = 2, \dots, T$. Then the lung motion vector of the patient can be estimated using a motion estimation model:

$$\mathbf{u}_{1 \rightarrow t}^P = \Theta(\mathbf{v}_{1 \rightarrow t}^P, \mathbf{u}_{1 \rightarrow t}^s, \mathbf{v}_{1 \rightarrow t}^s), \quad (11.15)$$

where $\Theta()$ represents the motion estimation operator. $\mathbf{u}_{1 \rightarrow t}^P$ can be transformed back to the patient space as

$$\mathbf{f}_{1 \rightarrow t}^P(\mathbf{x}) = g_{M \rightarrow P} \circ R_{M \rightarrow P}(\mathbf{x}) \mathbf{u}_{1 \rightarrow t}^P (G_{P \rightarrow M}(\mathbf{x} + \mathbf{f}_{P \rightarrow M}(\mathbf{x}))), \quad (11.16)$$

which can be applied to the input 3D image to generate a series of 3D images of the patient that match his/her chest motion signals. In the following, we introduce both linear and nonlinear estimation to determine the estimation model used in Eq. (11.15).

11.3.2 MOTION ESTIMATION MODELS

In this section, we introduce a kernel-principal component analysis (K-PCA)-based nonlinear statistical modeling method for estimating lung motion from chest surface motion. We first introduce the principal component analysis (PCA) method and then present the K-PCA-based estimation.

11.3.2.1 PCA model

The PCA algorithm can be used. According to PCA, a new vector can be calculated by:

$$\begin{bmatrix} \mathbf{u} \\ \mathbf{v} \end{bmatrix} = \begin{bmatrix} \bar{\mathbf{u}} \\ \bar{\mathbf{v}} \end{bmatrix} + \mathcal{M} \begin{bmatrix} \mathbf{b}_u \\ \mathbf{b}_v \end{bmatrix} \quad (11.17)$$

where \mathcal{M} is the matrix formed by the eigenvectors of the covariance matrix corresponding to the M largest eigenvalues. Thus given a new feature vector, $\mathbf{b} = [\mathbf{b}_u^T, \mathbf{b}_v^T]^T$, a lung respiratory motion field and the surface motion vector can be generated using Eq. (11.17). The underlying assumption of PCA is that a multidimensional Gaussian distribution is used to model these feature vectors:

$$p(\mathbf{b}) = \frac{1}{\sigma} \exp \left\{ -\sum_{m=1}^M b_m^2 / 2\lambda_m \right\}. \quad (11.18)$$

In order to estimate the lung respiratory motion field \mathbf{u}^P from the chest surface motion \mathbf{v}^P we need to solve the best the feature vector \mathbf{b} , so that \mathbf{v} calculated from \mathbf{b} using

Eq. (11.17) matches the patient's chest surface motion \mathbf{v}^P , and at the same time the prior distribution of Eq. (11.18) is maximized. The energy function is defined as

$$E(\mathbf{b}) = \|\mathbf{v}^P - \bar{\mathbf{v}} - \mathcal{M}_v \mathbf{b}\|^2 + \xi \sum_{m=1}^M b_m^2 / 2\lambda_m, \quad (11.19)$$

where \mathcal{M}_v is the matrix formed by the last rows of \mathcal{M} corresponding to $\bar{\mathbf{v}}$. After \mathbf{b} is estimated, the corresponding lung motion vector \mathbf{u}^P can be calculated by

$$\mathbf{u}^P = \Theta(\dots) = \bar{\mathbf{u}} + \mathcal{M}_u \mathbf{b}_P, \quad (11.20)$$

with \mathcal{M}_u as the top part of \mathcal{M} corresponding to the lung respiratory motion field \mathbf{u} .

11.3.2.2 Kernel-PCA model

K-PCA is a nonlinear statistical modeling method and can capture the variations of shapes more accurately than PCA. The basic idea of K-PCA is to compute PCA in a high-dimensional implicit mapping function of the motion vectors \mathbf{u} and \mathbf{v} . Let K denote the kernel matrix of N samples, $k_{ij} = k(\mathbf{u}_i^s, \mathbf{u}_j^s)$. K-PCA can be computed in a closed form by finding the first M eigenvalues and eigenvectors of K . Therefore given a motion vector \mathbf{u} , it can be projected onto the K-PCA space by $\lambda = A^T(\mathbf{k}(\mathbf{u}, \mathbf{u}_{i=1, \dots, N}^s) - \bar{\mathbf{k}})$, where $\bar{\mathbf{k}}$ is the mean of the kernel vectors, and $\mathbf{k}(\mathbf{u}, \mathbf{u}_{i=1, \dots, N}^s)$ is the vector obtained by calculating the kernel function between \mathbf{u} and \mathbf{u}_i^s , $i = 1, \dots, N$. Because in K-PCA the feature space is induced implicitly, reconstruction of a new vector \mathbf{u} from the feature vector λ is not trivial. Herein, Kwok, and Tsang's algorithm can be used for reconstruction (Kwok and Tsang, 2004).

11.3.2.3 Motion prediction using LS-SVM

Now that the lung motion vectors \mathbf{u}^s are projected onto the K-PCA space as λ^s , and the goal of motion estimation is to establish the relationship between the lung motion λ^s and chest surface motion $\mathbf{v}_{1 \rightarrow t}^P$. Because $\mathbf{v}_{1 \rightarrow t}^P$ has relatively low dimension, we did not apply K-PCA to it. Given N training sample-pairs, we can employ the least squares support vector machine (LS-SVM) model to estimate this relationship. In this case the estimator can be written as:

$$\lambda_t^s = \Theta(\mathbf{v}_{1 \rightarrow t}^P) + \epsilon. \quad (11.21)$$

Because the elements of λ_t^s are independent of each other in the K-PCA space, we can estimate each element separately using SVM:

$$\lambda = \mathbf{w}^T \varphi(\mathbf{v}) + \mathbf{b}, \quad (11.22)$$

where $\varphi(\mathbf{v})$ denotes a potential mapping function. \mathbf{w} is the weighting vector and \mathbf{b} is the shifting vector. The regularized cost function of the LS-SVM is given by An et al. (2007)

$$\min_{\xi} (\mathbf{w}, \boldsymbol{\epsilon}) = \frac{1}{2} \mathbf{w}^T \mathbf{w} + \frac{\gamma}{2} \sum_{i=1}^N \|\boldsymbol{\epsilon}_i\|^2 \quad (11.23)$$

s.t.

$$\lambda = \mathbf{w}^T \varphi(\mathbf{v}_i) + \mathbf{b} + \boldsymbol{\epsilon}_i, \quad i = 1, \dots, N, \quad (11.24)$$

where γ is referred to as the regularization constant. The Lagrangian method is utilized to solve the constrained optimization problem. Using typical radial basis function (RBF) kernel Π we get the parameters α and \mathbf{b} to estimate λ :

$$\lambda = \sum \alpha \Pi(\mathbf{v}, \mathbf{v}_i) + \mathbf{b}. \quad (11.25)$$

Notice that because different elements of the lung motion feature vector λ are independent, all of the elements of λ at different time-points are calculated by this model separately, similar to modeling the motion according to different lung capacity.

11.3.3 EXPERIMENTS

We introduced a method to estimate lung motion from a patient's 3D CT and chest signal after training the respiratory motion prediction models using 4D CT from a number of training samples. During intervention, 3D CT can be scanned on-site, and the key is to track the chest motion signals. Chest fiducial points and entire chest surface motion are commonly tracked. The difference is that for chest fiducial points four or more fiducial signals were used to track the chest motion, while for surface tracking much higher dimensional respiratory motion signals are used for estimation.

In the experiments, we used 4D CT datasets from 40 lung cancer patients undergoing radiotherapy planning. The images for each subject consist of 10 respiratory phases with the first and the last images being the exhale images and the fifth and the sixth the inhale images. The in-plane resolution of each image is $0.98 \text{ mm} \times 0.98 \text{ mm}$ and the slice thickness is 1.5 mm . One subject was randomly selected as the template, 29 were used for training and 10 were used for testing. The algorithm was implemented on a Dell workstation with Intel Core 2 Quad Processor Q9300 and 8 GB RAM.

The quantitative performance regarding how well the method recovers the longitudinal deformations for each testing image series is evaluated. For each testing subject, we register the 4D CT images and obtain the longitudinal deformations $\mathbf{f}_{1 \rightarrow t}^*(\mathbf{x})$. Then only the first frame and the chest surface motion signals extracted from the 4D CT images are used for estimation. After estimation, the estimated longitudinal deformations are denoted as $\hat{\mathbf{f}}_{1 \rightarrow t}(\mathbf{x}), t = 2, \dots, T$. The average lung respiratory motion estimation error for each subject can be calculated as

$$Err = \frac{1}{|\Omega|} \sum_{t=2, \dots, T} \sum_{\mathbf{x} \in \Omega} \left| \mathbf{f}_{1 \rightarrow t}^*(\mathbf{x}) - \hat{\mathbf{f}}_{1 \rightarrow t}(\mathbf{x}) \right|, \quad (11.26)$$

where Ω represents the domain of the voxels of the first time-point image of each subject. $|\Omega|$ is the number of voxels. The results showed that the estimation errors

using surface-based estimation method are between 0.92 and 1.63 mm, with an average of 1.17 mm, while the errors using the fiducial-based estimation method are between 1.22 and 2.16 mm, with an average of 1.61 mm.

Generally, the proposed surface-based estimation has higher performance than the estimation based on EM-tracked chest fiducials (He et al., 2010). The idea is that high-dimensional deformation is involved in the prediction problem, and compared to fiducial signals with four sensors high-dimensional chest surface motion would provide more accurate estimation. For the fiducial-based estimation, because of the limited number of fiducials, it may be feasible to predict the respiratory phases and to monitor the respiratory motion during intervention, but it may not have sufficient degrees-of-freedom to predict the precise shape and location of the internal anatomical structures, such as lung field, bone, diaphragm, tumor, etc.

In another evaluation, we calculated how well the shape of lung tumor is estimated. Fig. 11.6 shows some sample results. Fig. 11.6A is the inhale CT for a subject and Fig. 11.6B is the exhale CT. Their overlay is shown in Fig. 11.6C. To measure the tumor estimation accuracy, we estimated the inhale images from exhale images and compared quantitatively whether the estimated tumor shape in the estimated inhale phase matches that in the original inhale image. Fig. 11.6D–F shows the images of three other subjects with red curves (dark gray in print versions) as the manually marked tumor from the original inhale images, and the green curves

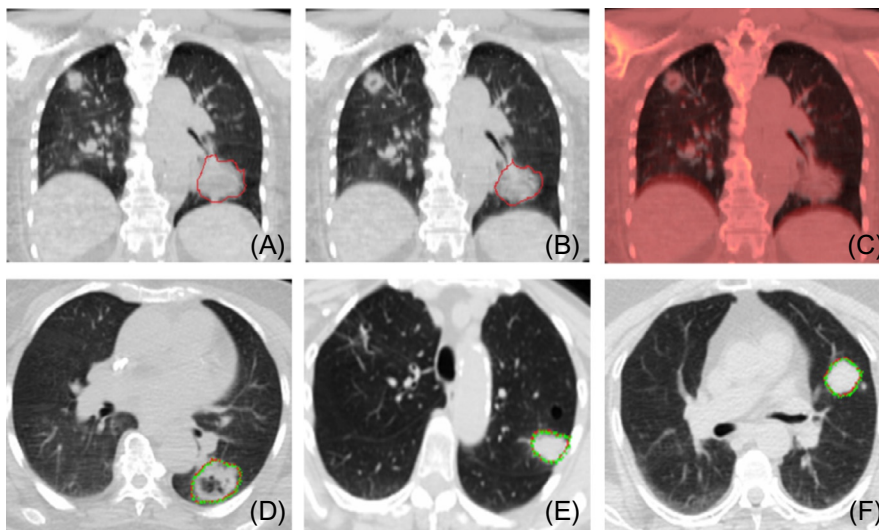


FIG. 11.6

Lung tumor estimation with dynamic modeling. (A) Exhale CT. (B) Inhale CT. (C) Overlaying (A) and (B). (D–F) Comparisons of tumor estimation between actual and estimated CT images.

show the estimated tumor shapes. We can see that the tumor positions and shapes under different respiratory phases can be estimated well. The DICE coefficient was used for quantitatively measuring estimation results of tumor positions. In our experiments, the average value of DICE coefficients over the 10 testing subjects is $88.1 \pm 2.8\%$ using the proposed algorithm, while the result is $82.6 \pm 5.7\%$ for fiducial-based estimation. Overall, these results demonstrate promising dynamic lung motion modeling.

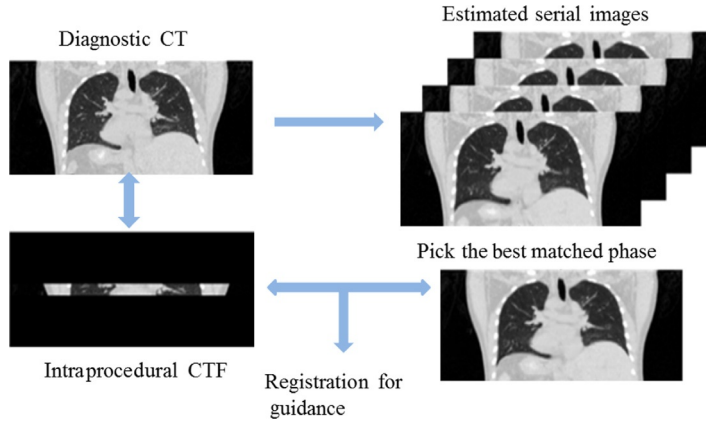
11.4 AN EXAMPLE FOR IMAGE-GUIDED INTERVENTION

A CT-fluoroscopy (CTF)-guided intervention system is introduced as an example of how the previously mentioned motion estimation can be applied in clinical settings. The objective is to register a preprocedural or diagnostic 3D CT image onto the real-time captured CTF image for 3D lung intervention guidance. Although there are many papers addressing the registration between 2D-2D, 3D-2D, or 3D-3D images in the literature (Yaniv et al., 2010; Cleary and Peters, 2010; Enquobahrie et al., 2008, 2007; Sun et al., 2006; Bouchet et al., 2001; Karnik et al., 2010; Park et al., 2010), they do not fit such a novel task: there is a limited number of slices for CTF, and the preprocedural 3D CT covers the entire or most of the lung region. To solve this problem, we customized the cubic B-spline model so that the deformation in the transverse plane is modeled using 2D B-spline, and the deformation in the z-direction is regularized using the general smoothness criterion. To improve registration accuracy, a respiratory motion compensation framework is incorporated into the registration procedure. Finally, parallel implementation allows for on-site application.

11.4.1 CTF GUIDANCE WITH MOTION COMPENSATION

Because the preprocedural inhale and exhale 3D CT images cover a larger lung region than the intraprocedural CTF that only has 4–10 slices, the current 3D-3D registration or 3D-2D registration algorithms do not fit this application. For example, the 3D cubic B-spline model is not applicable for the deformation in the z-direction given the limited number of slices for CTF. To solve this problem, we use the idea that the deformation model in the transverse plane should be handled differently from that in the z-direction. In addition, each CTF image is subject to a deformation from the inhale 3D CT, consisting of both respiratory motion and subtle anatomical deformation. Therefore the framework of motion compensation (MC) is utilized to better estimate the deformation between the current CTF image and the inhale 3D CT.

Fig. 11.7 illustrates the workflow of the CT-CTF registration algorithm with MC. First, the preprocedural or diagnostic CT scans are captured, and together with the intraprocedural CTF, they are used for estimating a series of images based on the previously introduced motion estimation methods. Then the best phase that matches the CTF image is picked and a fast registration is performed between the CTF and

**FIG. 11.7**

The workflow of the CT-CTF registration algorithm with motion compensation.

this selected image. The overlay of the registered 3D image on the CTF provides 3D guidance for the intervention. In this framework, the deformation between the phase-matched intermediate CT and the inhale CT is known, and our goal is to estimate the elastic deformation between this intermediate CT and the CTF. Compared to registering the diagnostic CT directly onto the CTF, the deformation between the intermediate CT and the CTF is much smaller because of the motion compensation, so the registration can be more accurate.

11.4.2 THE CT-CTF REGISTRATION ALGORITHM

The formulation of CT-CTF registration is in line with that of the common deformable image registration framework (Bai and Brady, 2009; Ferrant et al., 2000; Huang et al., 2006; Jacobson and Murphy, 2011; Johnson and Christensen, 2002; Mattes et al., 2003; Noblet et al., 2005; Rueckert et al., 2006, 2003, 1999; Shackleford et al., 2010; Sorzano et al., 2005; Warfield et al., 2002; Xue et al., 2010), with the objective of solving a deformation field $\mathbf{f}(\mathbf{x})$ to align the source 3D image $I_T(\mathbf{x})$ to the CTF image $I_{CTF}(\mathbf{x})$. The basic registration framework can be formulated by

$$\hat{\mathbf{f}} = \arg\min_{\mathbf{f}} (E_s(I_{CTF}, I_T, \mathbf{f}) + \lambda \mathfrak{R}(\mathbf{f})), \quad (11.27)$$

where $E_s(I_{CTF}, I_T, \mathbf{f})$ represents the image difference measure between the CTF image and the 3D CT under the current deformation field \mathbf{f} , and $\mathfrak{R}(\mathbf{f})$ is the regularization term for the deformation field. $\lambda > 0$ is the weighting coefficient of the regularization term. We use the modified cubic B-spline to model the deformations:

$$\mathbf{f}(\mathbf{x}) = \sum_{l=0}^3 \sum_{m=0}^3 B_l(u) B_m(v) c_{i+l,j+m,z}, \quad (11.28)$$

where B_l represents the l th basis function of the cubic B-spline. $\mathbf{x} = (x_1, x_2, x_3)$ is a voxel in the CTF image space Ω and c represents the deformation values of control points. Here, the control points are uniformly distributed on the voxel grids in the image domain, and $i = \lceil x_1/n_{x_1} \rceil - 1, j = \lceil x_2/n_{x_2} \rceil - 1, u = x_1/n_{x_1} - \lceil x_1/n_{x_1} \rceil$, and $v = x_2/n_{x_2} - \lceil x_2/n_{x_2} \rceil$. n_{x_1} and n_{x_2} are the pixel spacing between the control points in the x_1 and x_2 directions, respectively. Smaller control point spacing will result in a finer deformation but the computation time will increase slightly as the number of control points increases.

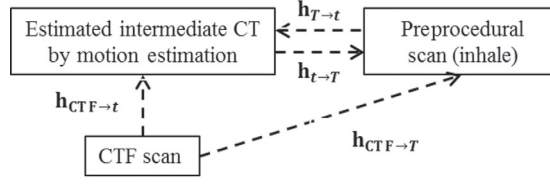
Notice that in Eq. (11.28), \mathbf{f} and c are defined in 3D space to model volumetric deformation, but the B-spline model is only used in the transverse plane. Therefore smoothness in the x - y plane is ensured due to the property of the B-spline. In the z -direction, an additional smoothness constraint is required, thus $\Re(\mathbf{f})$ in Eq. (11.27) can be defined as

$$\Re(\mathbf{f}) = \frac{1}{2} \sum_{\mathbf{x} \in \Omega} \|\partial \mathbf{f}(\mathbf{x}) / \partial x_3\|^2. \quad (11.29)$$

For image difference measurement, the sum of squared differences (SSD) of both image intensities and gradients are used. It has been shown that realistic deformation should not involve folding of the field and the neighboring voxels should not cross each other, and hence the local Jacobian determinant of the field should be positive. Therefore after registration the topology of the deformation field is checked (Karacali and Davatzikos, 2004).

In CT-CTF registration, the deformation field is defined on the CTF image space with a limited number of slices, hence the deformation on other slices of the 3D CT images can only be estimated. One way to estimate this deformation is to expand the deformation field outside the boundary of the CTF slices in the z -direction. However, if there is a large respiratory motion discrepancy between the preprocedural CT images and the CTF, a gradual transition or gap might be noticed. In order to estimate this deformation and accomplish more accurate registration, we propose to incorporate motion compensation into our CT-CTF registration.

Fig. 11.8 shows the framework for CT-CTF registration with MC, which consists of two steps. The first step is to generate a series of estimated intermediate respiratory phase CT images and to determine the intermediate CT that best matches the CTF. To do this, an inhale CT I_T is acquired in advance. Then CTF and I_T can be used to estimate an intermediate CT I_i using the motion estimation techniques described in Section 11.3. The second step is to register the inhale CT I_T with the CTF I_{CTF} by considering the respiratory differences. Denoting the deformation from the CTF to the phase-matched intermediate CT as $\mathbf{f}_{CTF \rightarrow i}$, the deformation of the whole procedure can be formulated as


FIG. 11.8

CT-CTF registration with motion compensation.

$$\mathbf{f} = \mathbf{f}_{t \rightarrow T} \circ \mathbf{f}_{\text{CTF} \rightarrow t}. \quad (11.30)$$

The deformation field from t to T , $\mathbf{f}_{t \rightarrow T}$, can be estimated through inverse operation. The intermediate CT image I_t can be generated by warping I_T using $\mathbf{f}_{t \rightarrow T}$. We can precalculate T intermediate CT images, and once a CTF is captured during the procedure, the phase-matched intermediate CT can be determined as the one that has the smallest least squares error (LSE) with the CTF after global rigid-body registration.

It can be seen that rather than registering the inhale CT onto the CTF image directly, we first deform the inhale CT I_T onto the respiratory phase-matched intermediate CT I_t and then further register it onto the CTF I_{CTF} . Because the deformation for respiratory motion $\mathbf{f}_{t \rightarrow T}$ is known, our goal is to estimate the deformation $\mathbf{f}_{\text{CTF} \rightarrow t}$. Compared to solving the deformation \mathbf{f} directly, the new strategy generates more accurate results because the unknown deformation $\mathbf{f}_{\text{CTF} \rightarrow t}$ is relatively small.

In fact, the phase-matched intermediate image I_t may not necessarily be used explicitly in the registration to prevent accumulation of image resampling errors. This is because $\mathbf{f}_{t \rightarrow T}$ is known, and we can embed it into the energy function in Eq. (11.27) as

$$\hat{\mathbf{f}} = \arg\min_{\mathbf{f}} (E_s(I_{\text{CTF}}, I_T, \mathbf{f}_{t \rightarrow T} \circ \mathbf{f}_{\text{CTF} \rightarrow t}) + \lambda \mathfrak{R}(\mathbf{f}_{\text{CTF} \rightarrow t})). \quad (11.31)$$

Alternatively, a linear interpolation can be used for motion estimation if both exhale I_1 and inhale I_T images are available. We can linearly scale the deformation $\mathbf{f}_{T \rightarrow 0}$ to estimate intermediate CTs I_t corresponding to respiratory phases between inhale and exhale. Let $T \in \mathbb{Z}^+$ be the number of estimated respiratory phases (ie, $T = 10$), and $t \in \mathbb{Z}^+$, $1 \leq t \leq T$, is an intermediate respiratory phase. The larger T is, the more intermediate CTs we can estimate. So the deformation from T to t , $\mathbf{f}_{T \rightarrow t}$ can be expressed as

$$\mathbf{f}_{T \rightarrow t} = \frac{T-t}{T} \mathbf{f}_{T \rightarrow 1}. \quad (11.32)$$

The deformation field from t to T , $\mathbf{f}_{t \rightarrow T}$, can be estimated through inverse operation.

11.4.3 EXPERIMENTS

A parallel and multiresolution strategy for the CT-CTF registration was implemented. Three resolutions were used and at each resolution images were partitioned into sub-blocks in the x - y plane, and then the registration of each block was performed in parallel. The finite differential method was used for optimization, and the change of the deformation value of each control point was calculated locally according to the B-spline. The advantage of using the finite differential method comes from being able to hierarchically adjust the number of control points involved in the registration. For example, in each iteration we only update the deformation of control points whose local image differences are ranked in a percentage over all the control points. We started from 50% and then gradually increased to 90% of control points in this hierarchical procedure. Using C++ language, we showed that the registration procedure finished within 2 s for the CT images of size $512 \times 512 \times 70$ and CTF image with size of $512 \times 512 \times 4$ on a quad-core Intel Xeon 2.8 GHz machine.

Fig. 11.9 shows an example of the CT-CTF registration algorithm with linear motion compensation. Fig. 11.9A is the CTF captured during breath holding,

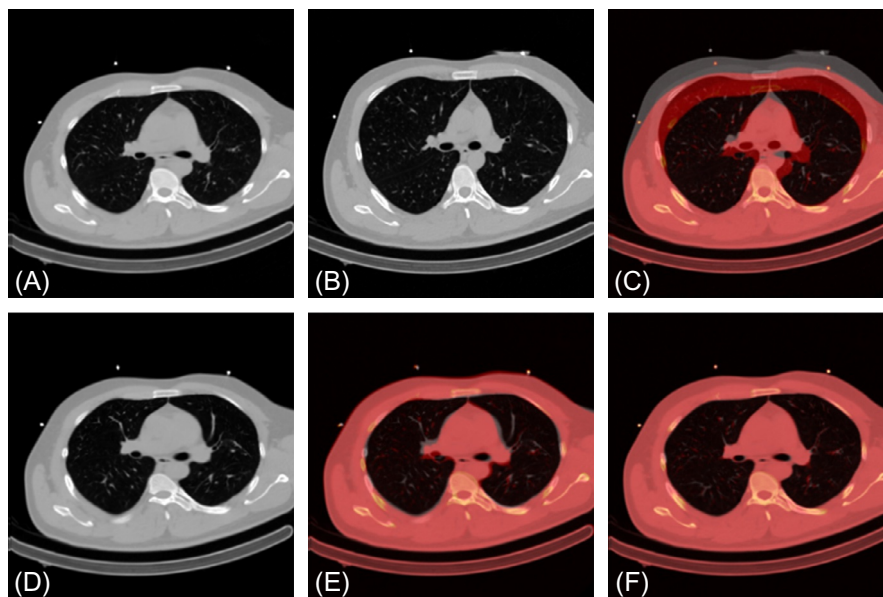


FIG. 11.9

An example of the CT-CTF registration algorithm with motion estimation. (A) CTF. (B) Inhale CT. (C) Overlay CTF (red) with inhale CT (gray scale) before registration. (D) The estimated intermediate image which matches the respiratory phase of CTF. (E) Overlay CTF (red) with (D) (gray scale). (F) The final registration result by overlaying the registered CT (gray scale) with CTF (red).

Fig. 11.9B is the inhale CT data, and Fig. 11.9C shows the overlay between these two images after global rigid-body registration. It is clearly seen that the discrepancy caused by the difference between breath-holding CTF image and inhale CT image is considerable. Using Eq. (11.32) a series of images between inhale and exhale are generated and the phase-matched intermediate CT image is chosen based on the least squares difference of the image intensity, shown in Fig. 11.9D. Fig. 11.9E shows the overlay of (A) and (D). It is shown that after applying motion compensation, the CT image matches CTF and a lot of respiratory motion-related deformation is removed. Fig. 11.9F gives the final registration results showing that the inhale CT image is nicely aligned with the CTF. Compared to registering (A) and (B) directly (the result is shown in Fig. 11.10), the deformation to be solved in our proposed framework is much smaller, rendering more accurate registration because the chance of being stuck in local minima during optimization is low.

We also applied the CT-CTF registration with MC to register the preprocedural inhale CT images onto CTFs and verified the registration by visual inspection for patient data during intervention. Fig. 11.11 shows examples of the overlay of the deformed inhale CT images (gray scale) with the intraprocedure CTFs (red; dark gray in print versions). From Fig. 11.11B it can be seen that the tumor and other parts (liver and lung field boundaries) are aligned well, while Fig. 11.11D and H show that the bones, airway, and lung field boundaries are also aligned well. We had gone through all the registered images by superimposing corresponding CTFs on them. The visual inspection by our radiologist showed that the aligned results on real-patient data are similar to those on the 4D CT data. For percutaneous lung

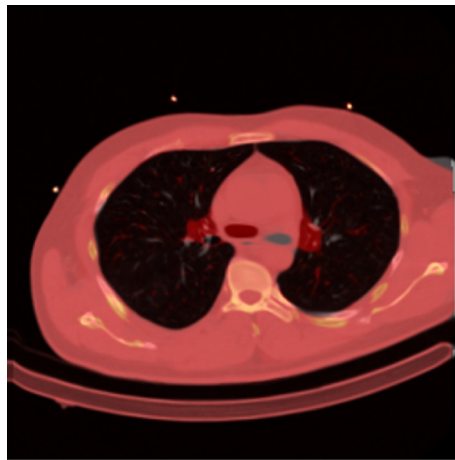
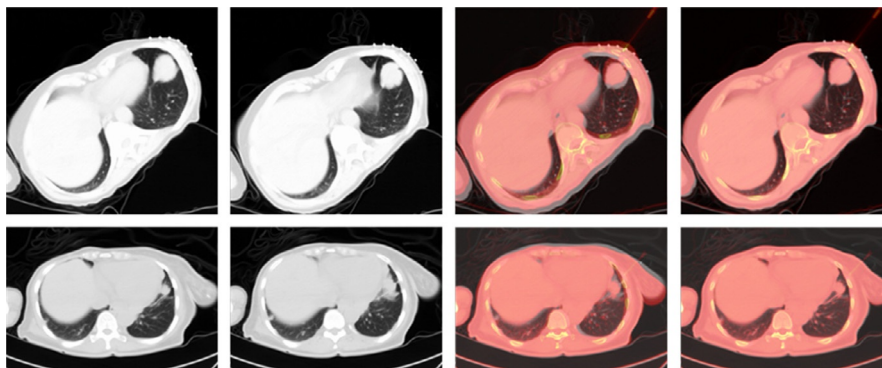


FIG. 11.10

The result by directly registering the CTF image in Fig. 11.9A and the CT image in Fig. 11.9B.

**FIG. 11.11**

Results of registered CT images by overlaying onto the CTF images of patient data collected from lung biopsy. From left to right: exhale CT image; inhale CT image; fused images before registration; fused images after registration.

intervention, it was reported that the average navigation error (3.3 mm) based on the registration between planning and confirmation images can successfully accomplish the intervention task (Yaniv et al., 2010). In our results, after motion compensation, the average registration error was 1.36 mm. We believe that the accuracy of the CT-CTF registration with MC is accurate enough for CT-guided percutaneous lung intervention. In future work, we plan to test the performance of the method during lung intervention (He et al., 2012).

11.5 CONCLUDING REMARKS

Using CT lung image motion compensation as an example, we showed that it is possible to estimate the dynamics of the lung by using available real-time chest motion signals. In addition to the necessary medical image processing techniques needed for motion compensation, we addressed the general question, ie, given the variability of the whole shape, how to estimate the shape from partially known information. In fact many engineering problems fall into this estimation category, and various prediction and regression models can be used. In this chapter, we showed that a general PCA model or K-PCA model can be used to project the high-dimensional signals and fields onto low-dimensional spaces. Then, Bayesian estimation or a support vector machine are used for estimation. Finally, using a CTF-guided intervention as an example, we illustrate how motion estimation can be applied in a clinical application. Future works include evaluating how the estimation

model can be more robust and reliable to handle different sizes and breathing patterns of the patients, and how to apply them in real-time estimation of location and shape of tumor for intervention and radiotherapy.

ACKNOWLEDGMENT

This work was supported by NIH grant 1R03EB018977 (ZX).

REFERENCES

- Alexander, D.C., Pierpaoli, C., Basser, P.J., Gee, J.C., 2001. Spatial transformations of diffusion tensor magnetic resonance images. *IEEE Trans. Med. Imaging* 20, 1131–1139.
- An, S.J., Liu, W.Q., Venkatesh, S., 2007. Fast cross-validation algorithms for least squares support vector machine and kernel ridge regression. *Pattern Recogn.* 40, 2154–2162.
- Bai, W., Brady, M., 2009. Regularized b-spline deformable registration for respiratory motion correction in pet images. *Phys. Med. Biol.* 54, 2719–2736.
- Bouchet, L.G., Meeks, S.L., Goodchild, G., Bova, F.J., Buatti, J.M., Friedman, W.A., 2001. Calibration of three-dimensional ultrasound images for image-guided radiation therapy. *Phys. Med. Biol.* 46, 559–577.
- Broadus, W.C., Gillies, G.T., Kucharczyk, J., 2001. Minimally invasive procedures. Advances in image-guided delivery of drug and cell therapies into the central nervous system. *Neuroimaging Clin. N. Am.* 11, 727–735.
- Cala, S.J., Kenyon, C.M., Ferrigno, G., Carnevali, P., Aliverti, A., Pedotti, A., Macklem, P.T., Rochester, D.F., 1996. Chest wall and lung volume estimation by optical reflectance motion analysis. *J. Appl. Physiol.* 81, 2680–2689.
- Cervino, L.I., Du, J., Jiang, S.B., 2011. MRI-guided tumor tracking in lung cancer radiotherapy. *Phys. Med. Biol.* 56, 3773–3785.
- Cleary, K., Peters, T.M., 2010. Image-guided interventions: technology review and clinical applications. *Ann. Rev. Biomed. Eng.* 12, 119–142.
- Cleary, K., Clifford, M., Stoianovici, D., Freedman, M., Mun, S.K., Watson, V., 2002. Technology improvements for image-guided and minimally invasive spine procedures. *IEEE Trans. Inform. Tech. Biomed.* 6, 249–261.
- de Gregorio, M.A., Laborda, A., Ortas, R., Higuera, T., Gomez-Arrue, J., Medrano, J., Mainar, A., 2008. Image-guided minimally invasive treatment of pulmonary arterial hypertension due to embolic disease. *Arch. Bronconeumol.* 44, 312–317.
- DeLucia, P.R., Mather, R.D., Griswold, J.A., Mitra, S., 2006. Toward the improvement of image-guided interventions for minimally invasive surgery: three factors that affect performance. *Hum. Fact.* 48, 23–38.
- Descoteaux, M., Collins, D.L., Siddiqi, K., 2008. A geometric flow for segmenting vasculature in proton-density weighted MRI. *Med. Image Anal.* 12, 497–513.
- DiMaio, S.P., Pieper, S., Chinzei, K., Hata, N., Haker, S.J., Kacher, D.F., Fichtinger, G., Tempany, C.M., Kikinis, R., 2007. Robot-assisted needle placement in open MRI: system architecture, integration and validation. *Comput. Aided Surg.* 12, 15–24.

- Ehrhardt, J., Werner, R., Schmidt-Richberg, A., Handels, H., 2011. Statistical modeling of 4d respiratory lung motion using diffeomorphic image registration. *IEEE Trans. Med. Imaging* 30, 251–265.
- Enquobahrie, A., Cheng, P., Gary, K., Ibanez, L., Gobbi, D., Lindseth, F., Yaniv, Z., Aylward, S., Jomier, J., Cleary, K., 2007. The image-guided surgery toolkit IGSTK: an open source C++ software toolkit. *J. Digital Imaging* 20 (1), 21–33.
- Enquobahrie, A., Gobbi, D., Turek, M., Cheng, P., Yaniv, Z., Lindseth, F., Cleary, K., 2008. Designing tracking software for image-guided surgery applications: IGSTK experience. *Int. J. Comput. Assist. Radiol. Surg.* 3, 395–403.
- Ferrant, M., Warfield, S., Nabavi, A., Jolesz, F., Kikinis, R., 2000. Registration of 3D intraoperative MR images of the brain using a finite element biomechanical model. In: *Medical Image Computing and Computer-Assisted Intervention—MICCAI 2000*, pp. 249–258.
- Frangi, A.F., Niessen, W.J., Vincken, K.L., Viergever, M.A., 1998. Multiscale vessel enhancement filtering. In: *Medical Image Computing and Computer-Assisted Intervention—MICCAI'98* 1496, 130–137.
- Hall, W.A., Liu, H., Martin, A.J., Truwit, C.L., 2001. Minimally invasive procedures: interventional MR image-guided neurobiopsy. *Neuroimaging Clin. N. Am.* 11, 705–713.
- Handels, H., Werner, R., Schmidt, R., Frenzel, T., Lu, W., Low, D., Ehrhardt, J., 2007. 4d medical image computing and visualization of lung tumor mobility in spatio-temporal CT image data. *Int. J. Med. Inform.* 76 (3), S433–S439.
- He, T., Xue, Z., Xie, W., Wong, S.T., 2010. Online 4-d CT estimation for patient-specific respiratory motion based on real-time breathing signals. *Med. Image Comput. Comput. Assist. Interv.* 13, 392–399.
- He, T., Xue, Z., Lu, K., Valdivia, Y.A.M., Wong, K.K., Xie, W., Wong, S.T., 2012. A minimally invasive multimodality image-guided (MIMIG) system for peripheral lung cancer intervention and diagnosis. *Comput. Med. Imaging Graph.* 36, 345–355.
- Hu, S., Hoffman, E.A., Reinhardt, J.M., Jun 2001. Automatic lung segmentation for accurate quantitation of volumetric X-ray CT images. *IEEE Trans. Med. Imaging* 20, 490–498.
- Huang, X., Paragios, N., Metaxas, D.N., 2006. Shape registration in implicit spaces using information theory and free form deformations. *IEEE Trans. Pattern Anal. Mach. Intell.* 28, 1303–1318.
- Jacob, A.L., Messmer, P., Kaim, A., Suhm, N., Regazzoni, P., Baumann, B., 2000. A whole-body registration-free navigation system for image-guided surgery and interventional radiology. *Investigat. Radiol.* 35, 279–288.
- Jacobson, T.J., Murphy, M.J., 2011. Optimized knot placement for b-splines in deformable image registration. *Med. Phys.* 38, 4579–4582.
- Johnson, H.J., Christensen, G.E., 2002. Consistent landmark and intensity-based image registration. *IEEE Trans. Med. Imaging* 21, 450–461.
- Karacali, B., Davatzikos, C., 2004. Estimating topology preserving and smooth displacement fields. *IEEE Trans. Med. Imaging* 23, 868–880.
- Karnik, V.V., Fenster, A., Bax, J., Cool, D.W., Gardi, L., Gyacskov, I., Romagnoli, C., Ward, A.D., 2010. Assessment of image registration accuracy in three-dimensional transrectal ultrasound guided prostate biopsy. *Med. Phys.* 37, 802–813.
- Klein, J.S., Schultz, S., Heffner, J.E., 1995. Interventional radiology of the chest: image-guided percutaneous drainage of pleural effusions, lung abscess, and pneumothorax. *Am. J. Roentgenol.* 164, 581–588.
- Klinder, T., Lorenz, C., Ostermann, J., 2010. Prediction framework for statistical respiratory motion modeling. *Med. Image Comput. Comput. Assist. Interv.* 13, 327–334.

- Kwok, J.T.Y., Tsang, I.W.H., 2004. The pre-image problem in kernel methods. *IEEE Trans. Neural Netw.* 15, 1517–1525.
- Lang, M.J., Greer, A.D., Sutherland, G.R., 2011. Intra-operative robotics: Neuroarm. *Acta Neurochirurg. Suppl.* 109, 231–236.
- Li, G., Ballangrud, A., Kuo, L.C., Kang, H., Kirov, A., Lovelock, M., Yamada, Y., Mechalakos, J., Amols, H., 2011. Motion monitoring for cranial frameless stereotactic radiosurgery using video-based three-dimensional optical surface imaging. *Med. Phys.* 38, 3981–3994.
- Lin, T., Cervino, L.I., Tang, X., Vasconcelos, N., Jiang, S.B., 2009. Fluoroscopic tumor tracking for image-guided lung cancer radiotherapy. *Phys. Med. Biol.* 54, 981–992.
- Lorigo, L.M., Faugeras, O.D., Grimson, W.E., Keriven, R., Kikinis, R., Nabavi, A., Westin, C.F., 2001. Curves: curve evolution for vessel segmentation. *Med. Image Anal.* 5, 195–206.
- Lu, W., Song, J.H., Christensen, G.E., Parikh, P.J., Zhao, T., Hubenschmidt, J.P., Bradley, J.D., Low, D.A., 2006. Evaluating lung motion variations in repeated 4d CT studies using inverse consistent image registration. *Int. J. Radiat. Oncol. Biol. Phys.* 66, S606–S607.
- Malladi, R., Sethian, J.A., Vemuri, B.C., 1995. Shape modeling with front propagation - a level set approach. *IEEE Trans. Pattern Anal. Mach. Intell.* 17, 158–175.
- Masutani, Y., MacMahon, H., Doi, K., 2001. Automated segmentation and visualization of the pulmonary vascular tree in spiral CT angiography: an anatomy-oriented approach based on three-dimensional image analysis. *J. Comput. Assist. Tomog.* 25, 587–597.
- Mattes, D., Haynor, D.R., Vesselle, H., Lewellen, T.K., Eubank, W., 2003. PET-CT image registration in the chest using free-form deformations. *IEEE Trans. Med. Imaging* 22, 120–128.
- Noblet, V., Heinrich, C., Heitz, F., Armspach, J.P., 2005. 3-d deformable image registration: a topology preservation scheme based on hierarchical deformation models and interval analysis optimization. *IEEE Trans. Image Process.* 14, 553–566.
- Osher, S., Sethian, J.A., 1988. Fronts propagating with curvature-dependent speed—algorithms based on Hamilton-Jacobi formulations. *J. Comput. Phys.* 79, 12–49.
- Pandya, S., Motkoski, J.W., Serrano-Almeida, C., Greer, A.D., Latour, I., Sutherland, G.R., 2009. Advancing neurosurgery with image-guided robotics. *J. Neurosurg.* 111, 1141–1149.
- Park, B.K., Kim, C.K., Choi, H.Y., Lee, H.M., Jeon, S.S., Seo, S.I., Han, D.H., 2010. Limitation for performing ultrasound-guided radiofrequency ablation of small renal masses. *Eur. J. Radiol.* 75, 248–252.
- Patriciu, A., Petrisor, D., Muntener, M., Mazilu, D., Schar, M., Stoianovici, D., 2007. Automatic brachytherapy seed placement under MRI guidance. *IEEE Trans. Biomed. Eng.* 54, 1499–1506.
- Rueckert, D., Sonoda, L.I., Hayes, C., Hill, D.L., Leach, M.O., Hawkes, D.J., 1999. Nonrigid registration using free-form deformations: application to breast MR images. *IEEE Trans. Med. Imaging* 18, 712–721.
- Rueckert, D., Frangi, A.F., Schnabel, J.A., 2003. Automatic construction of 3-d statistical deformation models of the brain using nonrigid registration. *IEEE Trans. Med. Imaging* 22, 1014–1025.
- Rueckert, D., Aljabar, P., Heckemann, R.A., Hajnal, J.V., Hammers, A., 2006. Diffeomorphic registration using b-splines. *Med. Image Comput. Comput. Assist. Interv.* 9, 702–709.
- Sadeghi Naini, A., Patel, R.V., Samani, A., 2010. Ct-enhanced ultrasound image of a totally deflated lung for image-guided minimally invasive tumor ablative procedures. *IEEE Trans. Biomed. Eng.* 57, 2627–2630.

- Santelli, C., Nezafat, R., Goddu, B., Manning, W.J., Smink, J., Kozerke, S., Peters, D.C., 2011. Respiratory bellows revisited for motion compensation: preliminary experience for cardiovascular MR. *Magn. Reson. Med.* 65, 1098–1103.
- Seibel, R.M., 1997. Image-guided minimally invasive therapy. *Surg. Endosc.* 11, 154–162.
- Seimenis, I., Tsekos, N.V., Keroglou, C., Eracleous, E., Pitris, C., Christoforou, E.G., 2012. An approach for preoperative planning and performance of mr-guided interventions demonstrated with a manual manipulator in a 1.5t MRI scanner. *CardioVasc. Interven. Radiol.* 35, 359–367.
- Seinstra, B.A., van Delden, O.M., van Erpecum, K.J., van Hillegersberg, R., Mali, W.P., van den Bosch, M.A., 2010. Minimally invasive image-guided therapy for inoperable hepatocellular carcinoma: what is the evidence today? *Insights Imaging* 1, 167–181.
- Shackelford, J.A., Kandasamy, N., Sharp, G.C., 2010. On developing b-spline registration algorithms for multi-core processors. *Phys. Med. Biol.* 55, 6329–6351.
- Shah, A.P., Kupelian, P.A., Willoughby, T.R., Meeks, S.L., 2011. Expanding the use of real-time electromagnetic tracking in radiation oncology. *J. Appl. Clin. Med. Phys.* 12, 34–49.
- Shamir, R., Freiman, M., Joskowicz, L., Shoham, M., Zehavi, E., Shoshan, Y., 2005. Robot-assisted image-guided targeting for minimally invasive neurosurgery: planning, registration, and in-vitro experiment. *Med. Image Comput. Comput. Assist. Interv.* 8, 131–138.
- Sluimer, I., Schilham, A., Prokop, M., van Ginneken, B., 2006. Computer analysis of computed tomography scans of the lung: a survey. *IEEE Trans. Med. Imaging* 25, 385–405.
- Smith, K.A., Kim, H.S., 2011. Interventional radiology and image-guided medicine: interventional oncology. *Semin. Oncol.* 38, 151–162.
- Sorzano, C.O.S., Thévenaz, P., Unser, M., 2005. Elastic registration of biological images using vector-spline regularization. *IEEE Trans. Biomed. Eng.* 52, 652–663.
- Sun, D., Willingham, C., Durrani, A., King, P., Cleary, K., Wood, B., 2006. A novel end-effector design for robotics in image-guided needle procedures. *Int. J. Med. Robot. Comput. Assist. Surg.* 2, 91–97.
- Sundaram, T.A., Avants, B.B., Gee, J.C., 2004. A dynamic model of average lung deformation using capacity-based reparameterization and shape averaging of lung MR images. presented at the MICCAI 2004.
- Tan, K.S., Saatchi, R., Elphick, H., Burke, D., 2010. Real-time vision based respiration monitoring system. In: *7th International Symposium on Communication Systems Networks and Digital Signal Processing (CSNDSP)*, 2010, pp. 770–774.
- Tokuda, J., Fischer, G.S., DiMaio, S.P., Gobbi, D.G., Csoma, C., Mewes, P.W., Fichtinger, G., Tempny, C.M., Hata, N., Jan 2010. Integrated navigation and control software system for MRI-guided robotic prostate interventions. *Comput. Med. Imaging Graph.* 34, 3–8.
- Ukimura, O., 2010. Image-guided surgery in minimally invasive urology. *Curr. Opin. Urol.* 20, 136–140.
- Vandemeulebroucke, J., Rit, S., Kybic, J., Clarysse, P., Sarrut, D., 2011. Spatiotemporal motion estimation for respiratory-correlated imaging of the lungs. *Med. Phys.* 38, 166–178.
- Wang, F., Vemuri, B.C., Eisenschenk, S.J., 2006. Joint registration and segmentation of neuroanatomic structures from brain MRI. *Acad. Radiol.* 13, 1104–1111.
- Warfield, S.K., Talos, F., Tei, A., Bharatha, A., Nabavi, A., Ferrant, M., Black, P.M., Jolesz, F.A., Kikinis, R., 2002. Real-time registration of volumetric brain MRI by biomechanical simulation of deformation during image guided neurosurgery. *Comput. Vis. Sci.* 5, 3–11.

- Westendorff, C., Hoffmann, J., Troitzsch, D., Dammann, F., Reinert, S., 2004. Ossifying fibroma of the skull: interactive image-guided minimally invasive localization and resection. *J. Craniofac. Surg.* 15, 854–858.
- Wu, G., Wang, Q., Lian, J., Shen, D., 2011. Estimating the 4d respiratory lung motion by spatiotemporal registration and building super-resolution image. *Med. Image Comput. Comput. Assist. Interv.* 14, 532–539.
- Xiaohua, C., Brady, M., Lo, J.L., Moore, N., 2005. Simultaneous segmentation and registration of contrast-enhanced breast MRI. *Inform. Process. Med. Imaging* 19, 126–137.
- Xue, Z., Shen, D., Davatzikos, C., 2006. Classic: consistent longitudinal alignment and segmentation for serial image computing. *NeuroImage* 30, 388–99.
- Xue, Z., Wong, K., Wong, S.T., 2010. Joint registration and segmentation of serial lung CT images for image-guided lung cancer diagnosis and therapy. *Comput. Med. Imaging Grap.* 34, 55–60.
- Yakar, D., Schouten, M.G., Bosboom, D.G., Barentsz, J.O., Scheenen, T.W., Futterer, J.J., 2011. Feasibility of a pneumatically actuated mr-compatible robot for transrectal prostate biopsy guidance. *Radiology* 260, 241–247.
- Yaniv, Z., Cheng, P., Wilson, E., Popa, T., Lindisch, D., Campos-Nanez, E., Abeledo, H., Watson, V., Cleary, K., Banovac, F., 2010. Needle-based interventions with the image-guided surgery toolkit (IGSTK): from phantoms to clinical trials. *IEEE Trans. Biomed. Eng.* 57, 922–933.
- Yeung, R.W., Xia, J.J., Samman, N., 2006. Image-guided minimally invasive surgical access to the temporomandibular joint: a preliminary report. *J. Oral Maxillofac. Surg.* 64, 1546–1552.
- Yim, Y., Hong, H., 2008. Correction of segmented lung boundary for inclusion of pleural nodules and pulmonary vessels in chest CT images. *Comput. Biol. Med.* 38, 845–857.